Statistical Reconstruction for Cosmic Ray Muon Tomography

Larry J. Schultz, *Member, IEEE*, Gary S. Blanpied, Konstantin N. Borozdin,
Andrew M. Fraser, *Senior Member, IEEE*, Nicolas W. Hengartner, Alexei V. Klimenko,
Christopher L. Morris, *Member, IEEE*, Chris Orum, and Michael J. Sossong

Abstract—**Highly penetrating cosmic ray muons constantly shower the earth at a rate of about 1 muon per cm^2 per minute. We have developed a technique which exploits the multiple Coulomb scattering of these particles to perform nondestructive inspection without the use of artificial radiation. In prior work [1]–[3], we have described heuristic methods for processing muon data to create reconstructed images. In this paper, we present a maximum likelihood/expectation maximization tomographic reconstruction algorithm designed for the technique. This algorithm borrows much from techniques used in medical imaging, particularly emission tomography, but the statistics of muon scattering dictates differences. We describe the statistical model for multiple scattering, derive the reconstruction algorithm, and present simulated examples. We also propose methods to improve the robustness of the algorithm to experimental errors and events departing from the statistical model.**

Index Terms—**Expectation maximization (EM), homeland security, iterative methods, tomography.**

I. INTRODUCTION

TOMOGRAPHIC methods are generally used to construct an image or model of an object from multiple projections taken from different directions. Here, we discuss a relatively new kind of tomography based on the scattering of cosmic ray muons. Coming from deep space, stable particles, mostly protons, continuously bombard the Earth. These particles interact with atoms in the upper atmosphere to produce showers of particles that include many short-lived pions which decay and produce longer-lived muons. Muons interact with matter primarily through the Coulomb force, having no nuclear interaction and radiating much less readily than electrons. They lose energy only slowly through electromagnetic interactions. Consequently, many of the muons arrive at the Earth's surface as highly penetrating charged radiation. The muon flux at sea level is about one muon per cm^2 per minute. As a muon moves through material, Coulomb scattering off of the charges
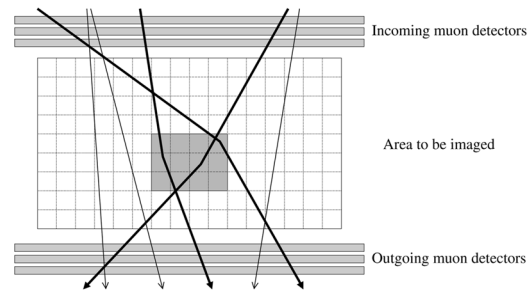
Fig. 1. Muon tomography concept. Muon detectors above and below the object provide the positions and angles of both incoming and outgoing muon tracks (shown by solid lines with arrows). The muons penetrating dense object (black tracks) scatter significantly stronger than muons going through air (gray tracks). From multiple track measurements both object geometry and electron density of the material can be reconstructed.

of subatomic particles perturb its trajectory. The total deflection depends on several material properties, but the dominant parameters are the atomic number, Z, of the nuclei and the material density. The trajectories are more strongly affected by *special nuclear material* (SNM) and materials that make good gamma ray shielding (such as lead and tungsten) than by the materials that make up more ordinary objects (such as water, plastic, aluminum, and steel). Each muon carries information about the objects that it has penetrated, and by measuring the scattering of multiple muons, one can probe the properties of these objects. In particular, one can detect high-Z objects amongst more typical low-Z and medium-Z matter [1]–[3].

Fig. 1 illustrates the *muon tomography* concept. A set of two or more planes of position sensitive muon detectors arranged above a volume to be imaged provides the position and angle of incoming muon tracks. These detectors measure muon position in two orthogonal coordinates. Muons pass through the volume and are scattered in a manner that depends on the materials through which they pass. Another set of muon detectors records outgoing muon positions and angles. Side detectors (not shown) may be used to detect more horizontally oriented muon tracks. The scattering angle of each muon is computed from the coincident incoming and outgoing measurements. Muon momentum is estimated from the slight scattering occurring in the detectors themselves. A description of our experimental implementation and discussion of the practical aspects of muon tracking appear in [4].

A discrete tomographic reconstruction of the volume of interest is performed based on the data provided by many muons. We use an instance of the iterative expectation maximization (EM) algorithm to find maximum likelihood estimates of
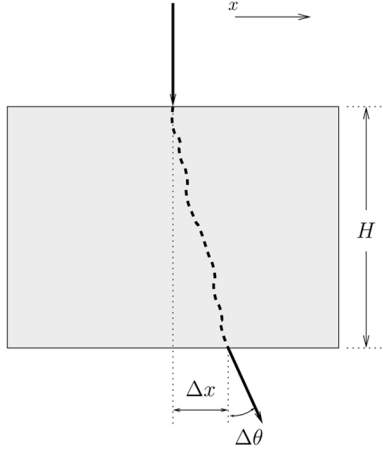
Fig. 2. Two-dimensional projection of scattering and displacement used to describe multiple Coulomb scattering. In this and other figures, the magnitude of scattering is greatly exaggerated.

density profiles of objects. Maximum likelihood is widely used in medical image reconstructions, in particular, for PET and SPECT reconstructions. Although muon tomography is similar to these methods, there are several important differences which preclude our use of standard methods developed for those applications. First, the measured signal—scattering angle—is stochastic, with mean equal to zero and standard deviation defined by the properties of the penetrated material. Second, cosmic-ray muons do not come from defined discrete directions, but rather have a broad angular distribution around zenith. Finally, muon trajectories are not straight; it is the bending that enables us to find the rough location of a strongly scattering object. While we used a Newton method to calculate maximum likelihood estimates of density profiles of simple geometries in earlier work [5], here we describe an EM algorithm which is flexible and computationally efficient and we illustrate its application to complex geometries.

II. MULTIPLE SCATTERING STATISTICAL MODEL

A. Single Layer of Homogeneous Material

A cosmic ray muon passing through material experiences multiple Coulomb scattering as illustrated in Fig. 2. The outgoing muon track may be characterized by the scattering angle $\Delta\theta$ and displacement Δx, taken relative to the orientation and position of the incident muon. The magnitude of scattering is exaggerated in the figure for illustrative purposes. Typical scattering angles are a few tens of mrads (1 mrad $\approx 0.06°$), and scattering angles of more than a few degrees are very uncommon.

The distribution of the central 98% of scattering angles may be approximated as a zero-mean Gaussian [6]

$$f_{\Delta\theta}(\Delta\theta) \cong \frac{1}{\sqrt{2\pi}\sigma_\theta} \exp\left(-\frac{\Delta\theta^2}{2\sigma_\theta^2}\right) \qquad (1)$$

though the actual distribution has heavier tails than a Gaussian. The width of the distribution may be expressed approximately in terms of material properties. Many researchers have presented empirically developed expressions for scattering as a function

of various material properties, as reviewed in [6]. A particularly simple form was presented by Rossi [7]

$$\sigma_\theta \cong \frac{15 \text{ MeV}}{\beta c p} \sqrt{\frac{H}{L_{\text{rad}}}}. \qquad (2)$$

Here, p is the particle momentum in MeV/c, H is the depth of the material, and L_{rad} is the radiation length of the material. βc is velocity, and we will assume $\beta = 1$. Radiation length decreases as atomic number and material density increase.

We establish a nominal muon momentum, p_0, and define the *scattering density* of a material with radiation length, L_{rad}, as

$$\lambda(L_{\text{rad}}) \equiv \left(\frac{15}{p_0}\right)^2 \frac{1}{L_{\text{rad}}}. \qquad (3)$$

The scattering density λ of a material thus represents the mean square scattering angle of muons with nominal momentum passing through a unit depth of that material. Values (in mrad² per centimeter) are about 3 for aluminum, 14 for iron, and 78 for uranium, for example.

So, the variance of scattering of a muon with momentum p passing through a material with scattering density λ and depth H is

$$\sigma_\theta^2 = \lambda H \left(\frac{p_0}{p}\right)^2. \qquad (4)$$

Let

$$p_r^2 = (p_0/p)^2 \qquad (5)$$

so

$$\sigma_\theta^2 = \lambda H p_r^2. \qquad (6)$$

The displacement Δx is correlated with the scattering angle $\Delta\theta$. Taken together, scattering angle and displacement provide information suggesting the position of local scattering contributors in a large volume, as suggested by the "kinks" in the paths in Fig. 1. The distribution of scattering angle and displacement may be characterized as jointly Gaussian [6], with zero mean and

$$\sigma_{\Delta x} = \frac{H}{\sqrt{3}}\sigma_{\Delta\theta} \qquad (7)$$

$$\rho_{\Delta\theta\Delta x} = \frac{\sqrt{3}}{2}. \qquad (8)$$

We may express the covariance matrix as

$$\Sigma \equiv \begin{bmatrix} \sigma_{\Delta\theta}^2 & \sigma_{\Delta\theta\Delta x} \\ \sigma_{\Delta\theta\Delta x} & \sigma_{\Delta x}^2 \end{bmatrix} = \lambda \begin{bmatrix} H & H^2/2 \\ H^2/2 & H^3/3 \end{bmatrix} p_r^2. \qquad (9)$$

Let

$$A \equiv \begin{bmatrix} H & H^2/2 \\ H^2/2 & H^3/3 \end{bmatrix} \qquad (10)$$

so

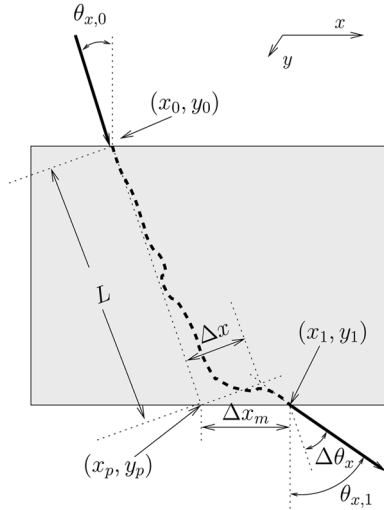$$\Sigma = \lambda A p_r^2. \qquad (11)$$

Fig. 3. Parameters used to adjust model for 3-D scattering.

In three dimensions, we may characterize scattering by considering a y coordinate orthogonal to x, and refer to scattering angles $\Delta\theta_x$ and $\Delta\theta_y$, and displacements Δx and Δy. Deflections into the x and y planes are independent and identically distributed [6]. The development above is based on a coordinate system which is oriented orthogonal to the direction of the incident muon. In a 3-D model we must account for 3-D path length and project displacement measurements to a plane orthogonal to the incident muon path. In Fig. 3, we illustrate a muon incident at a projected angle of $\theta_{x,0}$ from vertical. We ask the reader to imagine the associated projected angle $\theta_{y,0}$ in an orthogonal y coordinate directed out of the page.

The straight line extension of the muon path through the layer to the projected (unscattered) point x_p, y_p (i.e., the 3-D path length) is

$$L = H\sqrt{1 + \tan^2\theta_{x,0} + \tan^2\theta_{y,0}} \equiv HL_{xy}. \quad (12)$$

Define the outgoing muon x position and angle as $(x_1, \theta_{x,1})$, then let

$$\Delta\theta_x = \theta_{x,1} - \theta_{x,0}. \quad (13)$$

The measured x displacement would be computed as $x_m = x_1 - x_p$, but we must rotate this measurement into the plane orthogonal to the ray path and adjust for the 3-D path length. Define displacement as

$$\Delta_x = (x_1 - x_p)\cos(\theta_{x,0})L_{xy}\frac{\cos(\Delta\theta_x + \theta_{x,0})}{\cos(\Delta\theta_x)} \quad (14)$$

where the middle two terms account for 3-D path length and the final term projects the measurement to the proper orientation. Finally, redefine the covariance weightings as

$$A \equiv \begin{bmatrix} L & L^2/2 \\ L^2/2 & L^3/3 \end{bmatrix}. \quad (15)$$

Proceed in a similar fashion for the y scattering and displacement and (11) defines the covariance matrix for both x and y coordinate scat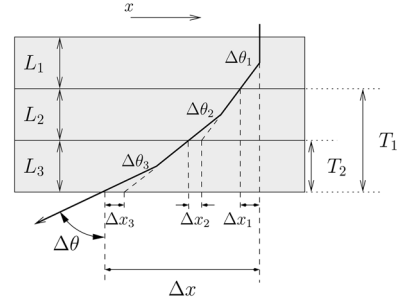tering. Scattering measurements are made independently in two orthogonal, horizontal coordinates. To simplify notation, we develop the analysis for only one coordinate. Combining the information from the two coordinates will be discussed later. We must note that the model is valid for "small" scattering angles and displacements. Second-order terms ignored in the derivation of the model may become significant for large angle scattering.

Fig. 4. Scattering through multiple layers of material.

B. Nonhomogeneous Volume Represented With 3-D Voxels

For a nonhomogeneous volume of material, we represent the density profile for purposes of reconstruction in terms of a linear combination of 3-D basis functions $\{\phi_1, \ldots, \phi_j, \phi_N\}$ with coefficients $\{v_1, \ldots, v_j, v_N\}$, i.e.,

$$\lambda(x, y, z) = \sum_j v_j \phi_j(x, y, z). \quad (16)$$

Though many choices exist for the basis functions, we restrict our attention to rectangular 3-D voxels. We will use λ_j to denote the coefficient of the jth basis function, i.e., the density in the jth voxel. One approach to expressing the distribution of scattering for a muon passing through a volume so represented would be to use continuous integrals of the form presented in [8] and recast the integrals in terms of the basis function representation. For voxels, however, we can use a more intuitive geometric development.

Considering Fig. 4, three layers (or voxels) are shown, with a ray passing through the stack, delivering observed information $\Delta\theta$ and Δx. "Hidden" scattering and displacement in the jth voxel are denoted $\Delta\theta_j$ and Δx_j, respectively. Again, the magnitude of scattering is exaggerated in the figure. We may relate observed to hidden data through the expressions

$$\Delta\theta = \Delta\theta_1 + \Delta\theta_2 + \Delta\theta_3 \quad (17)$$

$$\begin{aligned} \Delta x &= \Delta x_1 + L_2\tan(\Delta\theta_1) + \Delta x_2 \\ &\quad + L_3\tan(\Delta\theta_1 + \Delta\theta_2) + \Delta x_3 \\ &\approx \Delta x_1 + \Delta x_2 + \Delta x_3 + T_1\Delta\theta_1 + T_2\Delta\theta_2. \end{aligned} \quad (18)$$

Here, we rely on the assumption of small angle scattering in the second equation, and define T_j as the 3-D ray path length from the exit point of the jth voxel to the exit point from the reconstruction volume. More generally, for a ray passing through a set of voxels $\aleph$

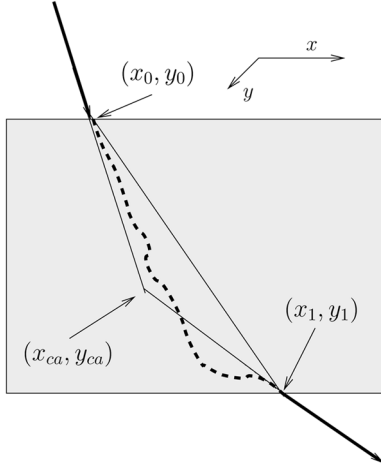$$\Delta\theta = \sum_{j \in \aleph} \Delta\theta_j \quad (19)$$

Fig. 5.   Using point of closest approach for path-length calculations.

$$\Delta x = \sum_{j \in \aleph} (\Delta x_j + T_j \Delta \theta_j). \tag{20}$$

Finally, we may express the covariance of aggregate scattering/displacement for the ith ray by first noting that, for the jth voxel

$$\Sigma_{ij} = \lambda_j A_{ij} p_{r,i}^2 \tag{21}$$

where

$$A_{ij} \equiv \begin{bmatrix} L_{ij} & L_{ij}^2/2 \\ L_{ij}^2/2 & L_{ij}^3/3 \end{bmatrix} \tag{22}$$

and L_{ij} is the path length of the ith ray through the jth voxel, defined to be zero for voxels not "hit" by the ray. Combining (19)–(22), we may write

$$\Sigma_i = p_{r,i}^2 \sum_{j \leq N} \lambda_j W_{ij}. \tag{23}$$

Here, N is the total number of voxels and we define the weight matrix

$$W_{ij} \equiv \begin{bmatrix} L_{ij} & L_{ij}^2/2 + L_{ij}T_{ij} \\ L_{ij}^2/2 + L_{ij}T_{ij} & L_{ij}^3/3 + L_{ij}^2 T_{ij} + L_{ij}T_{ij}^2 \end{bmatrix} \tag{24}$$

based on a simple but lengthy calculation [5] for the elements.

We must make some assumption about the unknown muon path in order to estimate ray path lengths through voxels. Referring to Fig. 5, our original method was to simply connect measured entry point (x_0, y_0) and exit point (x_1, y_1) with a straight line. For small angle scattering, there is little error in this assumption. It is clear, however, that this method biases the assumed path away from the true path for larger angle scatters. We observed blur in numerical testing due to this bias. A more accurate approximation begins with computation of the point of closest approach (PoCA) of incoming and outgoing tracks (x_{ca}, y_{ca}) [3]. Then, entry to PoCA to exit points are connected to estimate voxel path lengths. This approximation dramatically reduced blur in numerical tests (see Section IV).

Finally, define the data vector

$$D_i \equiv \begin{bmatrix} \Delta \theta_i \\ \Delta x_i \end{bmatrix} \tag{25}$$

and let D denote denote all of the measurements from M muons. We write the likelihood of the density profile λ as

$$P(D \mid \lambda) = \prod_{i \leq M} P(D_i \mid \lambda) \tag{26}$$

with factors

$$P(D_i \mid \lambda) = \frac{1}{2\pi |\Sigma_i|^{1/2}} \exp\left(-\frac{1}{2} D_i^T \Sigma_i^{-1} D_i\right). \tag{27}$$

One goal of this paper is to describe an efficient procedure for calculating an estimate, $\hat{\lambda}$, of the density profile that maximizes the likelihood. Our first approach via Newton-type methods for small simulated examples does not scale well to larger inversion problems because of the computation and storage requirements for the Hessian matrix [5]. In the next section, we describe an *EM* approach capable of dealing with practical sized problems.

C. Extensions for Experimental Effects

Real muon detectors exhibit finite position resolution. The incoming and outgoing muon tracks are characterized by angles and positions derived from track fits to multiple position measurements. Measurement errors thus propagate to the scattering angle and displacement measurements that constitute the dataset for muon tomography. We characterize the precision of a given detector by RMS error e_p. For a particular arrangement of detectors, the error matrix

$$E \equiv \begin{bmatrix} e_{\Delta\theta}^2 & e_{\Delta\theta\Delta x} \\ e_{\Delta\theta\Delta x} & e_{\Delta x}^2 \end{bmatrix} \tag{28}$$

may be defined based on how e_p propagates. See Schultz [5] for a calculation of this error matrix for a particular experiment.

Such error is relatively easy to deal with in iterative reconstruction methods. In our case, we may account for detector error by supplementing the covariance matrix of (23)

$$\Sigma_i = E + p_{r,i}^2 \sum_{j \leq N} (\lambda_j W_{ij}). \tag{29}$$

In this way, we reduce noise that would otherwise appear in reconstructions due to detector error. In fact, even when reconstructing simulated data wherein detectors are "perfect" we assume a very small e_p to avoid artifacts due to finite numerical precision. A more accurate model for detector error should account for momentum dependency, since one source of tracking error is scattering in the detectors themselves, and scattering decreases as particle momentum increases. If an estimate of individual muon momentum, $\hat{p}_i$, is available, then the error matrix $E_i(\hat{p}_i)$ could be estimated for each ray.

As is evident from (2), the width of multiple Coulomb scattering depends on the particle momentum. We accounted for different muon momenta by introducing the factor p_r^2 in (5). In practice, we do not know the muon momentum precisely but may estimate the momentum of an individual muon from measurements and the known spectrum of cosmic-ray muons. We

discuss methods of muon momentum measurement elsewhere [3], [4]. Here, we will assume that we have a good estimate of $\hat{p}_{r,i}^2$ for each muon.

III. ML/EM RECONSTRUCTION

The EM algorithm[1] relies on expressing the likelihood of the "incomplete" data in terms of the "complete" data, i.e., the observed data plus the *hidden* data.[2] In our application, the observed data $D = \{D_i : 1 \leq i \leq M\}$ is the measured scattering. The hidden data $H = \{H_{ij} : 1 \leq i \leq M \& 1 \leq j \leq N\}$ is the scattering angle and displacement of the ith muon by the jth voxel. Dempster, Laird and Rubin [9] described the algorithm in terms of the following auxiliary function:

$$Q_{\mathrm{DLR}} = \mathbb{E}_{H \mid D, \lambda^{(n)}}[\log(P(D, H \mid \lambda))]. \tag{30}$$

This function is the expected value of the log likelihood of both the observed and unobserved data, given the parameter vector λ with respect to the conditional distribution of H given D and the parameter vector $\lambda^{(n)}$. Each iteration of the algorithm consists of the following two steps.

E step: *Estimate* or characterize $P(H \mid D, \lambda^{(n)})$ the conditional distribution of the hidden data.

E step: *Maximize* the auxiliary function Q which is an expected value with respect to the distribution characterized in the E step.

In our case, since the hidden data determines the observed data uniquely, by using the simpler auxiliary function

$$Q(\lambda; \lambda^{(n)}) = \mathbb{E}_{H \mid D, \lambda^{(n)}}[\log(P(H \mid \lambda))] \tag{31}$$

we obtain the same sequence of estimates $\{\lambda^{(n)}\}_{n=1}^{N_{\mathrm{iter}}}$ that one would obtain by using Q_{DLR}. From the parameter estimate, $\lambda^{(n)}$, an iteration of the algorithm produces the new estimate, $\lambda^{(n+1)}$, by

$$\lambda^{(n+1)} = \arg\max_{\lambda} Q(\lambda; \lambda^{(n)}). \tag{32}$$

We start by noting that the probability distribution for scattering of a single muon through a single voxel follows simply from the statistical model for a single layer (Section II-A)

$$P(H_{ij} \mid \lambda) = \frac{1}{2\pi|\Sigma_{ij}|^{1/2}} \exp\left(-\frac{1}{2}H_{ij}^T\Sigma_{ij}^{-1}H_{ij}\right) \tag{33}$$

where Σ_{ij} is defined in (21). Since the unconditional distribution of scattering in each voxel is independent of the scattering in other voxels, the probability of the aggregate set of hidden

data is the product of the probability of each element. Therefore, the log likelihood may be written

$$\log(P(H \mid \lambda)) = \sum_{j \leq N}\sum_{i:L_{ij}\neq 0}\left(-\log\lambda_j - \frac{H_{ij}^T A_{ij}^{-1} H_{ij}}{2\lambda_j p_{r,i}^2}\right) + C \tag{34}$$

where C represents terms not containing λ. Taking the conditional expectation we write the Q function as

$$Q(\lambda; \lambda^{(n)}) = C + \sum_{j \leq N} Q_j(\lambda_j; \lambda_j^{(n)}) \tag{35}$$

with summands

$$Q_j(\lambda_j; \lambda_j^{(n)}) = -M_j \log\lambda_j - \frac{1}{2\lambda_j}\sum_{i:L_{ij}\neq 0} S_{ij}^{(n)}. \tag{36}$$

Here, M_j is the number of rays for which $L_{ij} \neq 0$ (i.e., the number of rays hitting the jth voxel), and $S_{ij}^{(n)}$ is defined

$$S_{ij}^{(n)} \equiv \mathbb{E}_{H \mid D, \lambda^{(n)}}\left[p_{r,i}^{-2}H_{ij}^T A_{ij}^{-1} H_{ij}\right]. \tag{37}$$

Setting the derivative with respect to λ_j of (36) to zero, we find the following iterative formula for maximizing the auxiliary function (M-step)

$$\lambda_j^{(n+1)} = \frac{1}{2M_j}\sum_{i:L_{ij}\neq 0} S_{ij}^{(n)}. \tag{38}$$

The quadratic form of S_{ij} guarantees positivity of $\lambda^{(n+1)}$. We also note that (38) represents a *mean* over rays hitting a voxel. The convenience of this form will be exploited in the next section.

It remains to calculate the conditional expectations S_{ij}. Let X denote the random variable $H_{ij} \mid D_i$. The expected value of the quadratic form $X^T A^{-1} X$ is

$$\mathbb{E}_{X^T A^{-1} X} = \mathrm{Tr}(A^{-1}\Sigma_X) + \mu_X^T A^{-1}\mu_X \tag{39}$$

where μ_X and Σ_X are the mean and covariance of X. Since D_i depends linearly on H_{ij} they are jointly Gaussian. The conditional distribution of H_{ij} given D_i is also Gaussian (a result from multivariate distribution theory; using this theory and the fact that H_{ij} and D_i each have zero mean, we find

$$\mu_X = \Sigma_{D_i H_{ij}}^T \Sigma_{D_i}^{-1} D_i, \tag{40}$$

$$\Sigma_X = \Sigma_{H_{ij}} - \Sigma_{D_i H_{ij}}^T \Sigma_{D_i}^{-1} \Sigma_{D_i H_{ij}}. \tag{41}$$

Here, Σ_{D_i}, the covariance of the observed data, is given by (29), and $\Sigma_{H_{ij}}$, the covariance of the hidden data element, may be expressed via (21). Rather than writing the covariance of observed-hidden data, $\Sigma_{D_i H_{ij}}$, explicitly, we can perform a simple (though lengthy) matrix calculation to show that

$$\Sigma_{D_i H_{ij}} A_{ij}^{-1} \Sigma_{D_i H_{ij}}^T = W_{ij}\left(p_{r,i}^2\lambda_j\right)^2. \tag{42}$$

---

[1]Although earlier papers by others described the algorithm, Dempster, Laird, and Rubin [9] coined the name *EM algorithm* and the standard terminology to define it.

[2]We develop our EM algorithm from a statistical perspective, but EM can be shown to be equivalent to scaled gradient descent [10], as well as a special case of incremental optimization transfer [11].

1) Gather measurements of scattering and momentum for each muon $i=1$ to M: $(\Delta\theta_x, \Delta\theta_y, \Delta x, \Delta_y, p_r^2)_i$.
2) Estimate geometry of interaction of each muon with each voxel $j=1$ to N: $(L,T)_{ij}$.
3) For each muon voxel pair, compute the weight matrix: W_{ij} using (24).
4) Initialize the scattering density in each voxel with a guess : $\lambda_{j,old}$.
5) Do until (stopping criteria)
   a) For each muon, compute $\Sigma_{D_i}^{-1}$ using (29) and taking the inverse.
   b) For each muon voxel pair, compute the conditional expectation terms: S_{ij} using (43).
   c) Compute $\lambda_{j,new}$ using (38)
   d) Set $\lambda_{j,old} = \lambda_{j,new}$ for all voxels.
6) End do

Fig. 6. Summary of the ML/EM algorithm for muon tomography.

Substituting results from (39)–(42) into (37), we find that

$$
\begin{aligned}
S_{ij}^{(n)} &= p_{r,i}^{-2}\mathrm{Tr}\left(A_{ij}^{-1}\Sigma_{H_{ij}} - A_{ij}^{-1}\Sigma_{D_iH_{ij}}^T\Sigma_{D_i}^{-1}\Sigma_{D_iH_{ij}}\right) \\
&\quad + p_{r,i}^{-2}D_i^T\Sigma_{D_i}^{-1}W_{ij}\Sigma_{D_i}^{-1}D_i\left(p_{r,i}^2\lambda_j^{(n)}\right)^2 \\
&= 2\lambda_j^{(n)} \\
&\quad + \left(D_i^T\Sigma_{D_i}^{-1}W_{ij}\Sigma_{D_i}^{-1}D_i - \mathrm{Tr}\left(\Sigma_{D_i}^{-1}W_{ij}\right)\right) \\
&\quad \times p_{r,i}^2\left(\lambda_j^{(n)}\right)^2
\end{aligned}
\tag{43}
$$

where we have used $\mathrm{Tr}(AB) = \mathrm{Tr}(BA)$ in the last step.

Finally, to incorporate both x and y coordinate scattering data, we simply use the average

$$
S_{ij}^{(n)} = \frac{S_{ij,x}^{(n)} + S_{ij,y}^{(n)}}{2}
\tag{44}
$$

in the update (38).

IV. NUMERICAL EXAMPLES AND ROBUST RECONSTRUCTION

To illustrate the ML/EM algorithm, we simulated a setup similar to that shown in Fig. 1. As a first validation test, we used a simple simulation designed to closely match our model. Single detector planes (rather than the 3 shown in the figure) were sized 2×2 m^2, and the vertical separation between top and bottom detectors was 1.1 m. These detectors perfectly recorded muon positions and angles. We used a simplified muon spectrum, with muons of momenta uniformly distributed from 500–10 000 MeV/c. Particles entered the volume at the upper detector plane at projected x,y angles uniformly spanning $[-\pi/4, \pi/4]$ from vertical. Muon multiple scattering and displacement were simulated according to the model of Section II. Objects were placed in the central $1.1 \times 1.1 \times 1.1$ m^3 portion of the volume as visualized in Figs. 7 and 8. We simulated three $10 \times 10 \times 10$ cm^3 cubes of materials tungsten,
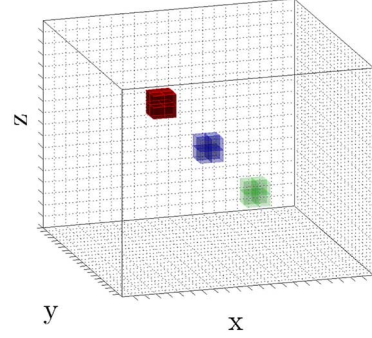

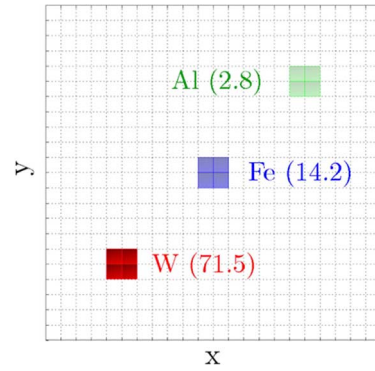Fig. 7. Perspective view of simulated objects.

Fig. 8. Overhead view of simulated objects.

iron, and aluminum, with scattering densities 71.5, 14.2, and 2.8, shown in red, blue, and green, respectively. We simulated 400 000 muons, incident on the upper detector stack, corresponding to about 10 min of exposure. About 160 000 of these muons missed the lower detector plane, leaving 240 000 for reconstruction. We used a voxel size of $5 \times 5 \times 5$ cm^3 for reconstruction and implemented the methods described in the previous section, assuming perfect knowledge of each muon's momentum. We started with a volume filled with air, and ran the algorithm for 100 iterations (sufficient for convergence of the block features).[3]

Results appear in Fig. 9. In this and other 3-D visualizations to follow, voxels with scattering density $[30, \infty]$ mrad^2 per centimeter are colored red, $[5,30)$ blue, and $[.5,5)$ green, roughly corresponding to high, medium, and low-Z material, respectively [3]. Visualized in this way, the reconstruction appears identical to the object scene. The averages of the reconstructed values for the 8 voxels corresponding to each of the three objects are (74.0, 14.7, 2.7) for the (W, Fe, Al) blocks, respectively. The fractional spreads (rms/mean) of the 8 voxels making up each cube are (12.6%, 13.2%, 12.1%). This result validates the inversion algorithm and implementation, given a match between simulation and inversion models. For comparison, we show, in Fig. 10, a reconstruction made from the same dataset but using the straight line voxel path-length calculation rather the PoCA

[3]Rather than use regularization, some stop iterative ML algorithms before convergence to control noise. We do not address this issue here.
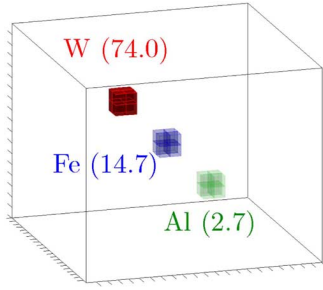
Fig. 9. Reconstruction of Gaussian scattering simulation with path lengths estimated assuming two lines connected at the PoCA point.
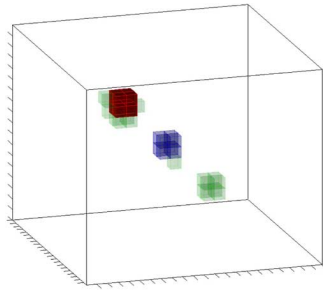

Fig. 11. Reconstruction of simulated data using scattering with non-Gaussian tails.

Fig. 10. Reconstruction of Gaussian scattering simulation with path lengths estimated assuming a single straight line.

Fig. 12. Reconstruction of simulated data with non-Gaussian tails via the median method.

method (see Section II-B). Note the slight blur around the tungsten and iron blocks.

Next, we resimulated the same scene using the GEANT4 [12] Monte Carlo package. GEANT4 implements a more complete, accurate, and validated model for multiple scattering. This model includes a more refined calculation of the width of the central Gaussian portion of the scattering distribution, implementation of the heavy tails, and the simulation of the energy loss of muons as they pass through material. We also used a muon event generator which replicated the sea-level angular and momentum distribution of cosmic ray muons. We still assumed that detectors were perfect in this simulation, with perfect knowledge of each muon's momentum, and we did not include cosmic ray electrons or track secondary particles.

Results appear in Fig. 11. Averages of voxels values corresponding to (W, Fe, Al) blocks are (674.4, 63.4, 5.4), respectively. These values are much too high and the misclassification of several of the medium and low Z areas is apparent. Normalizing the reconstruction by dividing all voxel values by approximately 4 to produce a correct average voxel value for the medium-Z voxels does not produce correct values for high and low-Z voxels or eliminate all misclassification. The cause of this effect is a small percentage of the muons scattering in a manner not well described by the Gaussian model.

We claimed that the central 98% of the projected angular distribution of scattering is well approximated as Gaussian. About 2% of all muons scatter to angles that are large relative to the statistical model described here. Because we attend to the *square* of scattering angles, the effect can be dramatic. Muon scatterings that fall in these tails produce density estimates that are too large. Moreover, other processes such as decay of a muon within the instrument of Fig. 1 or significant detector errors may
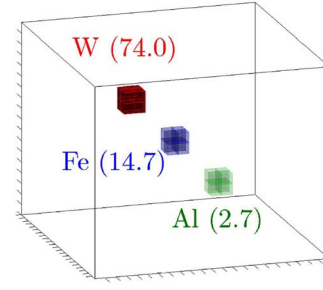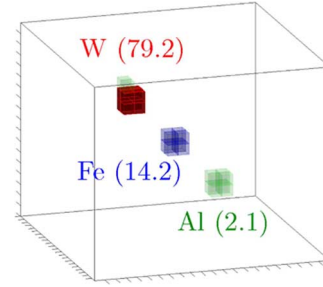
be erroneously recorded as very large angle scattering events (though these sources were not present in our simulation). This can happen anywhere in the volume, and tends to generate single voxels with unreasonably large scattering density. We have considered revising our statistical model to account for these processes, but have not yet found a simple way to do so. Instead, we have experimented with an altered algorithm, starting with the observation that the update rule (38) is a *mean* over rays passing through each voxel. To make the algorithm tolerant to non-Gaussian data, we replace (38) with

$$\lambda_j^{(n+1)} = \frac{1}{2}\text{median}_{i:L_{ij}\neq0}S_{ij}^{(n)} \qquad (45)$$

i.e., take the *median* rather than the *mean* over rays to update each voxel. We will term the update rule (45) the *median method* and (38) the *mean method*.

Results using the median method appear in Fig. 12. Voxel averages for (W, FE, Al) regions are (79.2, 14.2, 2.1), respectively, with fractional spreads of (21.5%, 26.3%, 23.2%). Clearly, using the median update rule improves the robustness of the inversion algorithm. though with some loss of efficiency relative to Gaussian data/mean update. Although this empirical result suggests that the median update rule is better than the mean update rule, we do not yet completely understand how it affects efficiency, monotonicity, positivity, and other intrinsic advantages of the mean method.

These simple block scenes were designed for validation of the statistical model and inversion algorithm and are not illustrative of the potential practical applications of cosmic ray muon tomography. Though it is outside the scope of this paper to delve deeply into such applications, we conclude with a more interesting scene. We produced a detailed GEANT4 simulation of a passenger van. An illustration of the major components with the
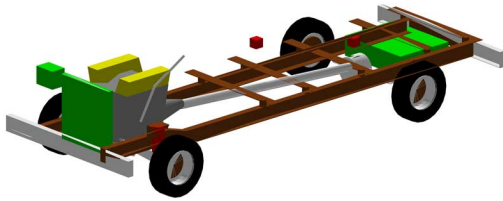
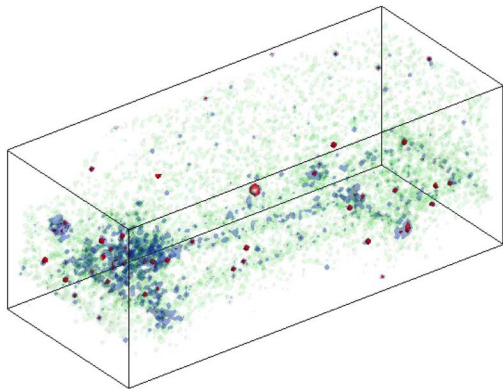Fig. 13. Illustration of major objects in a simulated passenger van.

Fig. 14. Reconstruction of 1 min of simulated muon exposure of the passenger van via the *mean* method.
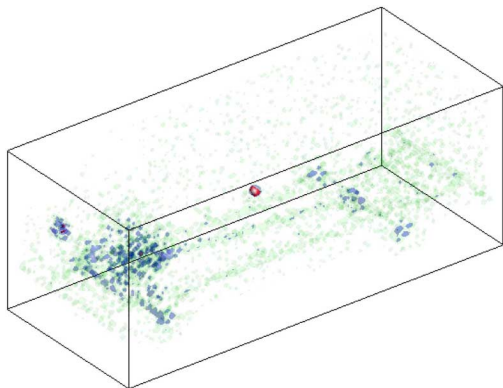

Fig. 15. Reconstruction of the passenger van scene via the *median* method.

van body cut away appears in Fig. 13. The red block in the center of the illustration represents a $10 \times 10 \times 10$ cm^3 solid piece of tungsten, a proxy for a high-Z threat object. In this case we used simulated detector planes located on the four long sides of the scene to take advantage of more horizontally oriented muons. We simulated 1 minute of cosmic ray muon exposure and performed reconstructions from the data using $5 \times 5 \times 5$ cm^3 sized voxels. In Figs. 14 and 15, we show visualizations of reconstructions made using both the mean and median EM methods, respectively.

The effect of non-Gaussian data is quite apparent in the mean method reconstruction of this scene, manifested as red spots scattered over the image. In the median reconstruction, these artifacts are entirely gone, and the denser components of the van (engine, battery, drive train) show up as green (low-Z) or blue (medium-Z), while the threat object stands out as red.

V. CONCLUDING REMARKS

Implementing cosmic ray muon tomography required developing new information processing algorithms. We have described a statistical tomographic inversion algorithm specifically designed to mine the information present from passive cosmic ray muons which are constantly passing through terrestrial objects.

Each iteration of the algorithm took about 2 s for the block scenes (32 000 voxels, 240 000 muons), and about 1 s for the van scene (240 000 voxels, 90 000 muons) on a standard PC for either the mean or median update rule. Since each voxel is updated independently at each iteration, parallel implementation is quite feasible and could provide for near real-time reconstruction.

Future work includes the addition of regularization to our algorithm. We are currently modifying it to evaluate the effect of quadratic and edge preserving penalty terms as in [13]. With colleagues we have constructed a large muon tracker [4] that is providing the means to validate the algorithm on experimental data. Finally, we are evaluating the efficacy of cosmic ray muon tomography for various homeland security inspection applications. Two key parts of the evaluation are establishing automatic detection methods and evaluating exposure time, detection probability, and false alarm rates. For this work we are considering additional real world effects such as finite detector resolution and estimated muon momentum, with key aspects validated against experiments. We anticipate that detector spatial resolution will have little effect on reconstructions, since muon detectors have been built that exhibit good resolution (a few hundred microns rms [4]) relative to voxel sizes and scattering angles of interest. The achievable precision of the muon momentum estimate will affect required exposure times [5], [3].
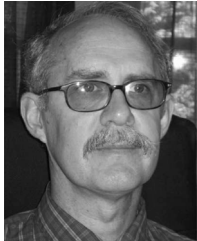
ACKNOWLEDGMENT

REFERENCES

[1] K. Borozdin, G. Hogan, C. Morris, W. Priedhorsky, A. Saunders, L. Schultz, and M. Teasdale, "Radiographic imaging with cosmic-ray muons," *Nature*, vol. 422, p. 277, Mar. 2003.

[2] W. Priedhorsky, K. Borozdin, G. Hogan, C. Morris, A. Saunders, L. Schultz, and M. Teasdale, "Detection of high-z objects using multiple scattering of cosmic ray muons," *Rev. Sci. Instrum.*, vol. 74, no. 10, pp. 4294–4297, Oct. 2003.

[3] L. Schultz, K. Borozdin, J. Gomez, G. Hogan, J. McGill, C. Morris, W. Priedhorsky, A. Saunders, and M. Teasdale, "Image reconstruction and material z discrimination via cosmic ray muon radiography," *Nucl. Instrum. Meth. A*, vol. 519, pp. 687–694, Mar. 2004.

[4] J. Green *et al.*, "Optimizing the tracking efficiency for cosmic ray muon tomography," in *Proc. IEEE Nuclear Science Symp. Conf. Rec.*, Oct. 2006, pp. 286–288.

[5] L. Schultz, "Cosmic ray muon radiography," Ph.D. dissertation, Portland State Univ., Portland, OR, 2003.

[6] S. Eidelman *et al.*, "Review of particle physics," *Phys. Lett.*, vol. B592, p. 1, 2004.

[7] B. Rossi, *High Energy Particles*. Englewood Cliffs, NJ: Prentice-Hall, 1952.

[8] U. Schneider and E. Pedroni, "Multiple coulomb scattering and spatial resolution in proton radiography," *Med. Phys.*, vol. 21, no. 11, pp. 1657–1663, Nov. 1994.

[9] A. Dempster, N. Laird, and D. Rubin, "Maximum likelihood from incomplete data via the EM algorithm," *J. Roy. Statist. Soc. B*, vol. 39, pp. 1–78, 1977.

[10] Y. Vardi, L. Shepp, and L. Kaufman, "A statistical model for positron emission tomography," *J. Amer. Statist. Assoc.*, vol. 80, no. 389, pp. 8–20, Mar. 1985.

[11] S. Ahn, J. Fessler, D. Blatt, and A. Hero, "Convergent incremental optimization transfer algorithms: Application to tomography," *IEEE Trans. Med. Imag.*, vol. 25, no. 5, pp. 283–296, Mar. 2006.

[12] J. Allison, "Geant4 developments and applications," *IEEE Trans. Nucl. Sci.*, vol. 53, no. 1, pp. 270–278, Feb. 2006.

[13] I. Elbakri and J. Fessler, "Statistical image reconstruction for polyenergetic x-ray computed tomography," *IEEE Trans, Med. Imag.*, vol. 21, no. 2, pp. 89–99, Feb. 2002.

Andrew M. Fraser (SM'79) received the Ph.D. degree in physics from the University of Texas at Austin in 1988 with a dissertation on algorithms for analyzing chaotic signals.

He is a member of the machine learning team of the ISR division at Los Alamos National Laboratory, Los Alamos, NM. Before graduate school, he designed bipolar memories at Fairchild Semiconductor, and from 1989 to 2005, he was on the faculty of Portland State University, Portland, OR.

Nicholas W. Hengartner received the B.A. degree in mathematics from the Universite Laval, Quebec, QC, Canada, in 1987, the M.S. degree in statistics from the University of Waterloo, Waterloo, ON, Canada, in 1988, and the Ph.D. degree in statistics from the University of California, Berkeley, in 1993.

Upon graduation, he joined the Department of Statistics, Yale University, New Haven, CT, as an Assistant Professor, and was promoted to Associate Professor in 1999. In 2002, he joined the Statistical Science Group at Los Alamos National Laboratory, Los Alamos, NM. He is active in academic outreach activities, and in 2004, was given an Adjunct Professor in the Department of Statistics at Simon Fraser University, Burnaby, BC, Canada. His research interests are in trans-disciplinary application of statistics, stochastic modeling, and information science to physics, epidemiology, and large-scale socio-technical simulations.

Larry J. Schultz (M'01) received the M.S. and Ph.D. degrees in electrical engineering from Portland State University, Portland, OR, in 2000 and 2003, respectively.

He has been a technical staff member in the Applied Modern Physics Group at Los Alamos National Laboratory, Los Alamos, NM, since 2001, specializing in signal and image processing for national security applications.

Alexei V. Klimenko received the B.S. and M.S. degrees in electrical engineering from the Moscow Institute of Steel and Alloys (Moscow University of Technology), Moscow, Russia, in 1998 and 1999, respectively, and the M.S. and Ph.D. degrees in nuclear physics from Old Dominion University, Norfolk, VA, in 2001 and 2004, respectively.

From 2004 to 2006, he was a Postdoctoral Research Associate at Los Alamos National Laboratory, Los Alamos, NM. He is currently a Staff Scientist at Passport Systems, Inc., Acton, MA, specializing in modeling and threat detection algorithm development for nonintrusive cargo screening systems.

Gary S. Blanpied received the Ph.D. degree in 1977 based partially on nuclear physics research using 800-MeV protons at the linac at Los Alamos National Laboratory, Los Alamos, NM (at that time, the C. P. Anderson Meson Physics facility).

He has been a Professor of physics at the University of South Carolina, Columbia, since 1979.

Christopher L. Morris (M'06) received the B.S. degree from Lehigh University, Lehigh, PA, in 1969, and the Ph.D. degree from the University of Virginia, Charlottesville, in 1973.

He is currently a technical staff member at Los Alamos National Laboratory, Los Alamos, NM, specializing in nuclear physics and national security research.

Dr. Morris is a Fellow of the American Physical Society (1986) and a Fellow of Los Alamos National Laboratory (1996).

Chris Orum received the B.A. degree in chemistry from the University of Oregon, Eugene, and the M.S. and Ph.D. degrees in mathematics from Oregon State University, Corvallis, in 1996 and 2004, respectively.

He is currently a Postdoctoral Research Associate at Los Alamos National Laboratory, Los Alamos, NM.

Konstantin N. Borozdin received the M.S. degree in experimental nuclear physics from the Moscow Engineering Physics Institute in 1988, Moscow, Russia, and the Ph.D. degree in astrophysics and radioastronomy from the Moscow Space Research Institute in 1995.

He is currently a technical staff member with the Space Science and Applications Group, Los Alamos National Laboratory, Los Alamos, NM. He has been at Los Alamos since 1998, working in the fields of astrophysics, physical modeling, information technologies, radiation detection, and national security applications.

He received an Order of Merit medal for his involvement in the Mir-Kvant space experiments in 1997.

Michael J. Sossong received the B.S., M.S., and Ph.D. degrees in physics from the University of Illinois at Urbana-Champaign, Urbana, in in 1998, 2000, and 2005, respectively.

He is a technical staff member working on the particle transport applications team in the Applied Science and Methods Development Group, Applied Physics (X) Division, Los Alamos National Laboratory, Los Alamos, NM. He specializes in nuclear and particle physics, particle transport simulation, information processing, and applications to national security.